ADVANCED FUNCTIONAL MATERIALS
www.afm-journal.de

# A Scanning Microwave Impedance Microscopy Study of $\alpha$-$In_2Se_3$ Ferroelectric Semiconductor

*Lin Wang,* Han Chen, Mingfeng Chen, Yinfeng Long, Kai Liu, and Kian Ping Loh**

**Van der Waals ferroelectric semiconductors, which encompass both ferroelectricity and semiconductivity, have garnered intensive research interests for developing novel non-volatile functional devices. Previous studies focus on ferroelectricity characterization and device demonstration, with little attention paid to the fundamental electronic properties of these materials and their functional structures, which are essential for both device design and optimization. In this study, scanning microwave impedance microscopy (sMIM) is utilized to investigate the ferroelectric semiconductor of $\alpha$-phase indium selenide ($\alpha$-$In_2Se_3$) and its synaptic field effect transistors. $\alpha$-$In_2Se_3$ nanoflakes of varying thicknesses are visualized through capacitive signal detection, whose responses are consistent with finite element simulations manifesting dependence on both flake thickness and its semiconductor property. sMIM spectroscopy performed on $\alpha$-$In_2Se_3$-based metal-oxide-semiconductor (MOS) structures reveals typical MOS capacitance-voltage characteristics, with additional hysteresis arising from the ferroelectric switching of $\alpha$-$In_2Se_3$. The local conductance state changes of synaptic $\alpha$-$In_2Se_3$ ferroelectric semiconductor transistors (FeSFET) in response to gate voltage stimuli are effectively detected by in situ sMIM, in good agreement with electrical device transport properties. This work deepens the understanding of ferroelectric semiconductor physics toward their practical device application.**

## 1. Introduction

The discovery of van der Waals (vdW) ferroelectric materials have stimulated considerable interests in ferroelectric-based in-memory computing and neuromorphic electronics.[1–8] Compared with oxides ferroelectric counterparts, the ability to retain ferroelectricity down to monolayer thickness addresses the issues related to critical thicknesses for ferroelectricity.[9–12] Moreover, their semiconducting character makes possible the construction of ferroelectric semiconductor field effect transistors (FeSFETs), where the layered ferroelectric semiconductor serves as channel material as opposed to gate dielectric, further alleviating the charge trapping and gate leakage current issues confronting the complex gate stack in conventional ferroelectric field effect transistors (FeFETs).[13] $\alpha$-$In_2Se_3$ is among the most widely studied vdW ferroelectric materials.[14–19] FeSFETs based on $\alpha$-$In_2Se_3$ have demonstrated large memory window and tremendous potential for ultrafast neuromorphic computing with superior controllability and suppressed cycle-to-cycle variation.[13,17–18] Conventional studies are mainly focused on the ferroelectricity characterization of materials and electrical transport measurement of devices. Consequently, there is less understanding on the switching behavior of a ferroelectric semiconductor, which can convolute both dipole switching and modulation of carrier density.[19] Ferroelectric semiconductors possess distinct electronic properties from conventional wide-gap ferroelectrics or non-ferroelectric semiconductors. It is critical to gain a good understanding of their material physics for developing devices toward real application. Meanwhile, measurements of devices' electrical transport characteristics inherently render averaged response of the device over large area with little insight into its local electrical properties, and consequently are incapable of understanding the differences in electronic properties between devices caused by spatial inhomogeneities such as doping and structural defects.[20–22] Derived from atomic force microscopy (AFM), scanning microwave impedance microscopy (sMIM) delivers a microwave signal at a few GHz to the tip apex to interact with the sample, and consequently probes its local electrical properties from analyzing the reflected microwave response.[23] sMIM offers outstanding versatility to electrically image diverse samples covering insulators, semiconductors, conductors, and even buried structures.[24–34]

In this work, we applied sMIM to characterize ferroelectric semiconductor $\alpha$-$In_2Se_3$ nanoflakes and its metal-oxide-semiconductor (MOS) structures, and probe the evolution of

L. Wang, H. Chen, M. Chen, Y. Long, K. Liu
School of Mechanical Engineering
Shanghai Jiao Tong University
Shanghai200240, China
E-mail: lin_wang@sjtu.edu.cn

K. P. Loh
Department of Applied Physics
The Hong Kong Polytechnic University
Hong Kong 999077, China
E-mail: kploh@polyu.edu.hk

The ORCID identification number(s) for the author(s) of this article can be found under https://doi.org/10.1002/adfm.202316583



**DOI: 10.1002/adfm.202316583**

channel conductance state of $\alpha$-$In_2Se_3$-based FeSFETs in a non-invasive manner. The capacitive sMIM signal (sMIM-C) component decreases with thickness for $\alpha$-$In_2Se_3$, and saturates for thickness beyond 100 nm, which reflects the thickness-dependent depletion situation of the flakes and is consistent with our finite element simulations. sMIM-C spectroscopy performed on $\alpha$-$In_2Se_3$ MOS structure reveals typical MOS-like capacitance-voltage (*C-V*) characteristics that are distinct from conventional ferroelectrics, with additional hysteresis arising from ferroelectric switching of $\alpha$-$In_2Se_3$. Furthermore, the in situ sMIM characterization of the high resistance state (HRS) and low resistance state (LRS) states of $\alpha$-$In_2Se_3$ synaptic device correlates well with its electrical transport result, evidencing the capability of sMIM as a convenient technique in quantitatively characterizing local electrical properties of ferroelectric neuromorphic devices.

## 2. Results and Discussion

### 2.1. Ferroelectricity Characterization of $\alpha$-$In_2Se_3$

$\alpha$-$In_2Se_3$ can exhibit either rhombohedral or hexagonal crystal structures, referred to as 2H ($P6_3mc$ space group) and 3R ($R3m$ space group) phases, respectively. Both structures are non-centrosymmetric and possess coupled out-of-plane and in-plane ferroelectricity. 2H $\alpha$-$In_2Se_3$ was used in this study (**Figure 1a**), as confirmed by the Raman spectrum, which reveals vibration peaks at 90, 104, 180, and 195 $cm^{-1}$ (Figure 1b; Figure S1; Table S1, Supporting Information). Piezoresponse force microscopy (PFM) was used to characterize the ferroelectric properties of $\alpha$-$In_2Se_3$. In Figure 1d–f, distinct ferroelectric domains are disclosed on the exfoliated flake with contrary out-of-plane PFM responses, where the 180-degree difference in the PFM phase indicates opposite polarization directions. The polarization switching of $\alpha$-$In_2Se_3$ is illustrated by the hysteresis loops of PFM phase and amplitude versus DC bias (Figure 1g,h). The PFM image (Figure 1i) reveals reversed PFM phase in the region undergoing a poling process, demonstrating the manipulation of $\alpha$-$In_2Se_3$ polarization orientation. Notably, no topography changes are observed, indicating that the observed phenomenon is primarily due to polarization switching rather than other processes (Figure S2, Supporting Information).

### 2.2. sMIM Characterization of $\alpha$-$In_2Se_3$ Nanoflakes

A schematic of the AFM-derived sMIM setup is illustrated in **Figure 2a**. During sMIM operation, the excitation microwave signal is transmitted to the tip apex to interact with the sample. The reflected microwave signal contains the information of the admittance/impedance of the tip-sample system, which depends on the local permittivity and conductivity of the sample of study. Consequently, the variation of the electronic properties results in changes of the reflected microwave signal, which is then detected by the radio frequency electronics module and processed into sMIM output, that is, real (sMIM-R) and imaginary (sMIM-C) components of the tip-sample impedance.

In this work, the changes in sMIM signal with the conductivity of $\alpha$-$In_2Se_3$ film on different substrates ($Si/Al_2O_3$ and Au film) are simulated through finite element analysis (FEA). As shown in Figure 2b (see also Figure S3, Supporting Information), the sMIM-C signal increases monotonically with the film conductivity, and saturates at the insulating and conductive limit, with the most sensitive region present between the two regimes. In contrast, the sMIM-R signal, being an indicator of the effective loss of the tip-sample interaction, approaches zero in the low and high conductivity limit of the sample, and peaks at an intermediate conductivity of 5 S $m^{-1}$.

We began by examining the ability of sMIM to detect $\alpha$-$In_2Se_3$ flakes exfoliated on conductive substrates. Figure 2c,d shows the topography and sMIM images, respectively (see Figures S4 and S5, Supporting Information for more results). $\alpha$-$In_2Se_3$ flakes of varying thicknesses are unambiguously detected and differentiated from the Au film in the sMIM-C channel. When the probe is in contact with Au film, the sMIM-C signal is the highest because the Au film serves as a ground plane terminating all the electric fields. In contrast, the $\alpha$-$In_2Se_3$ flakes yield smaller sMIM-C signals due to their relatively low conductivity and their dielectric property (see Figure S6, Supporting Information). To derive a scaling relationship, the sMIM-C signals difference between Au substrate and $\alpha$-$In_2Se_3$ nanosheets are extracted and plotted as a function of flake thickness. In Figure 2e, a quasi-inverse relationship of sMIM-C signal with thickness of $\alpha$-$In_2Se_3$ is observed below the thickness of 100 nm (see Figure S7, Supporting Information). However, with further increased thickness, the sMIM-C signal deviates from the inverse relationship. Assuming a constant permittivity of $\alpha$-$In_2Se_3$ for the investigated thickness range[29] and a weak conductivity of the depleted region, this trend agrees well with our numerical FEA simulations. Particularly, when the $\alpha$-$In_2Se_3$ flake becomes sufficiently thick, the free carriers within the flake are no longer fully depleted and the flake possesses a finite conductivity, leading to deviation from the thickness scaling relationship of the sMIM-C signal. These results demonstrate the importance of intrinsic semiconductor nature in understanding the material physics of vdW ferroelectrics.

### 2.3. sMIM Characterization of $\alpha$-$In_2Se_3$ Domains and MOS Structures

Next, we provide evidence of the distinct sMIM responses exhibited by opposite $\alpha$-$In_2Se_3$ domains. **Figure 3a,b** showcase the PFM phase and sMIM-C image, respectively, of an $\alpha$-$In_2Se_3$ flake after undergoing a poling process (additional corresponding results can be found in Figures S9 and S10, Supporting Information). It is evident that the opposing ferroelectric domains yield contrasting sMIM-C responses, indicating different material conductivities resulting from polarization modulation. This observation reveals the fundamental principle underlying $\alpha$-$In_2Se_3$ nonvolatile FeSFETs. The line profile in Figure 3c demonstrates a conductance evolution width of 147 nm across the domain wall, primarily determined by the diameter of the tip apex, which is consistent with previous findings in the literature. [30,35]

Before delving into the device study, we investigate the electronic properties (i.e., *C-V* characteristics) of $\alpha$-$In_2Se_3$-based MOS structures, which constitute the essential functional structure of $\alpha$-$In_2Se_3$ FeSFETs. To obtain the equivalent of the *C-V* plot, we record the sMIM signal on flakes exfoliated onto a

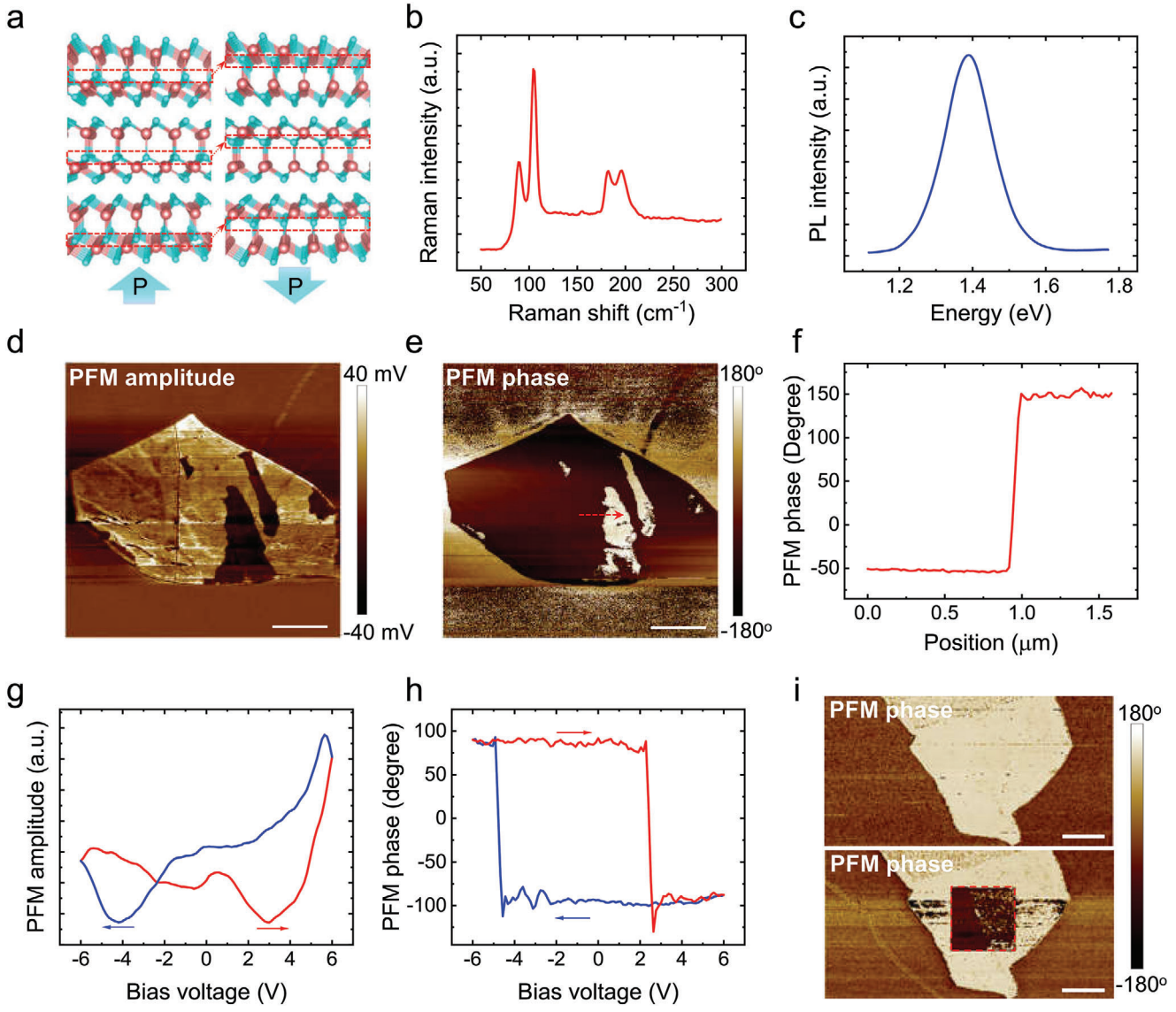


**Figure 1.** Material and ferroelectricity characterization of $\alpha$-$In_2Se_3$. a) Schematic atomic structure of 2H $\alpha$-$In_2Se_3$ in its two distinct polarization states. The Se positions corresponding to two distinct polarization states are indicated by red dashed rectangles. b) Raman spectrum of $\alpha$-$In_2Se_3$ under laser illumination of 532 nm wavelength peaking at 90, 104, 180, and 195 $cm^{-1}$, corresponding to $E^2$, $A_1$(LO + TO), $A_1$(LO), and $A_1$(LO) phonon modes of $\alpha$-$In_2Se_3$, respectively. c) Photoluminescence spectrum of an $\alpha$-$In_2Se_3$ flake under 633 nm excitation shows peak at 1.39 eV (wavelength of 892.7 nm), suggesting its semiconducting property. d,e) Representative out-of-plane PFM amplitude and phase images displaying opposite ferroelectric polarization within the scanned $\alpha$-$In_2Se_3$ nanoflake. Scale bars are 2 μm. f) PFM phase profile along the dashed line indicated in (e) shows a 180-degree difference for opposite polarization orientation. g,h) Hysteretic behavior of out-of-plane PFM response as a function of tip bias voltage for a flake of 37 nm thickness, manifesting ferroelectric polarization switching. The flake is exfoliated onto a 50 nm thick Au film. An AC voltage of 1000 mV amplitude was used for excitation. i) PFM phase images before and after poling the center area by +8 V tip bias, giving rise to opposite PFM phases. Scale bars are 2 μm.

degenerately doped Si substrate as a function of sample bias. A 6 nm thick $Al_2O_3$ layer is deposited on the sample surface to form the MOS structure (Figure 3d). As shown in Figure 3e (also refer to Figure S11, Supporting Information), the $\alpha$-$In_2Se_3$-based structure exhibits a hysteretic sMIM-C spectrum, resembling the classic *C-V* properties of MOS structures, albeit with additional hysteresis. The reduced capacitive signal with decreasing DC bias correlates well with the n-type conduction of $\alpha$-$In_2Se_3$, indicating an increasing depletion of the channel resulting in decreased sample capacitance. The observed hysteresis is attributed to the ferroelectric switching process. It is worth noting that interfacial charges in the MOS structure may also play a role in determining its *C-V* characteristics and the resultant device behaviors. However, careful analysis has shown that their effect is overshadowed by the polarization switching of the material.[18]

Regarding the differences in switching voltage across different samples in PFM and sMIM, these variations can be attributed to factors such as flake thickness, inserted insulating layer, surface oxide layer, AC voltage, and even the type of probe used. For instance, the larger tip radius of the sMIM probe compared to

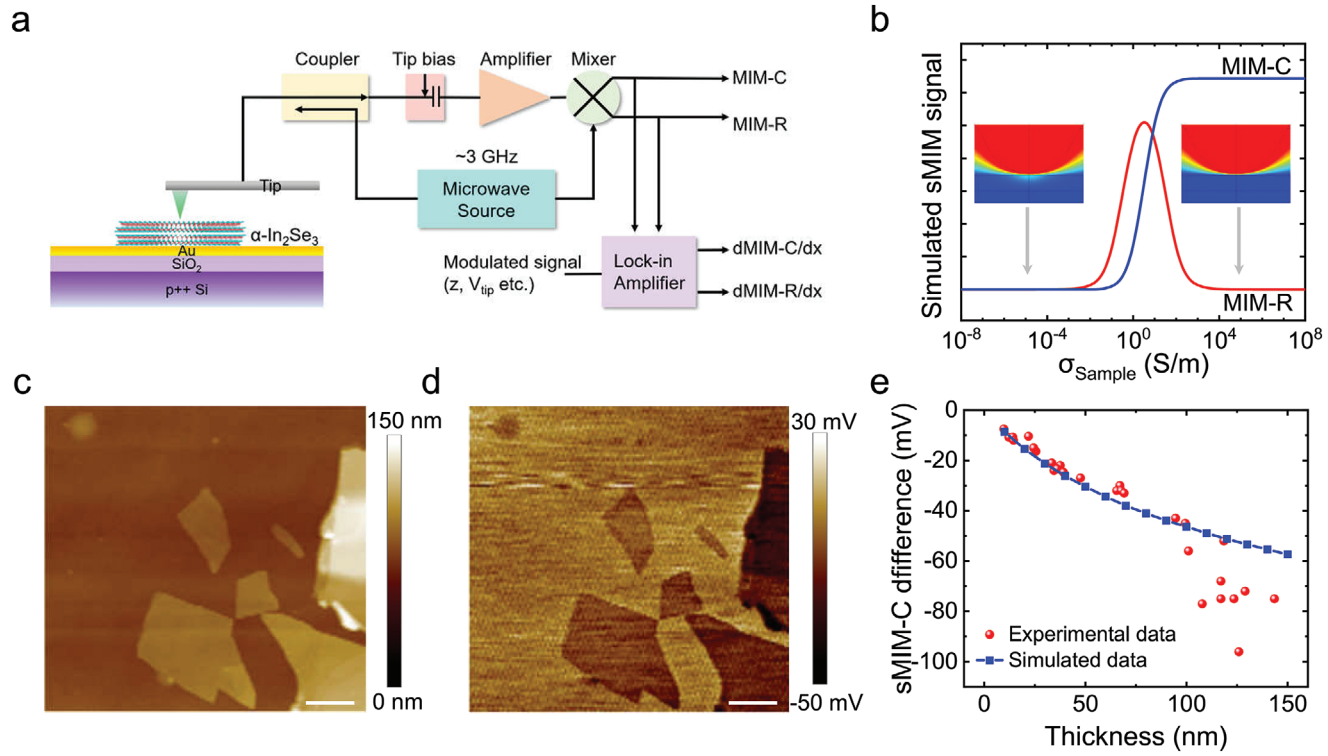


**Figure 2.** sMIM characterization of $\alpha$-$In_2Se_3$ nanoflakes. a) Experimental schematic of the sMIM setup. b) Simulated sMIM response as a function of the conductivity of a 33 nm thick $\alpha$-$In_2Se_3$ nanosheet placed on Au substrate. The insets show the calculated quasi-static potential distribution for two different $\alpha$-$In_2Se_3$ conductivities. c,d) Representative topography and corresponding sMIM-C images recorded on $\alpha$-$In_2Se_3$ flakes on Au film/Si substrate. Scale bars are 2 μm. e) Extracted experimental and simulated sMIM-C signal (difference between Au and $\alpha$-$In_2Se_3$) in dependence of the $\alpha$-$In_2Se_3$ flake thickness. The sMIM-C signal is quasi-inversely proportional to the thickness of $\alpha$-$In_2Se_3$ below 100 nm.

that in PFM may require a relatively large bias voltage for polarization switching. By superposing a 90 kHz AC modulating voltage on the sample, we acquire and display the characteristic of d(sMIM-C)/dV versus bias voltage in Figure 3f, which exhibits hysteresis with two peaks corresponding to the polarization switching bias voltage. We note that these voltage-dependent capacitive responses are distinct from those of typical insulating ferroelectric PZT (Figure S11f, Supporting Information) due to the interplay of the semiconductor nature of $\alpha$-$In_2Se_3$ and the polarization switching. In principle, the semiconductor-based MOS configuration determines the basic shape of the *C-V* curve, while the ferroelectric switching property leads to bias voltage hysteresis. These findings contribute to a better understanding of the device physics based on vdW ferroelectric semiconductors.

### 2.4. sMIM Characterization of $\alpha$-$In_2Se_3$ FeSFETs

Back-gated $\alpha$-$In_2Se_3$ FETs were fabricated based on nanosheets exfoliated onto a Si substrate ($p^{++}$ doped) covered with an $Al_2O_3$ layer of 50 nm thickness grown by atomic layer deposition (ALD). *C-V* measurement reveals a permittivity of 7.2 for the $Al_2O_3$ layer, thus the gate dielectric corresponds to an equivalent oxide thickness (EOT) of 27.1 nm (Figure S12, Supporting Information), allowing a large reduction of the device operation voltage. A schematic of the device structure is given in **Figure** 4a. Ti/Au was used for source and drain electrodes for low-resistance contact (See Experimental section for fabrication details). An additional encapsulating layer of 15-nm $Al_2O_3$ was deposited on the sample to serve as a protecting layer. Besides, it can largely improve the device performance in the aspects of on-state current and current on/off ratio, owing to the reduced surface scattering associated with the high-$\kappa$ dielectric environment and electron doping effect of $Al_2O_3$ (Figure S13, Supporting Information).[13]

We have fabricated devices using nanoflakes with thickness in the 20 to 50 nm range (Figure S14, Supporting Information). The transfer characteristics of a representative FeSFET are plotted in Figure 4b in the −8 to 8 V gate voltage ($V_{gs}$) range at different drain-source bias ($V_{ds}$ = 0.01, 0.05, 0.1 V). The device shows typical n-type conduction behaviors, as can be judged from the increased channel current with gate potential. The channel current on/off ratio exceeds $10^5$, which is underestimated due to the system detection limit of the device off-state current (≈20 pA). The output curves ($I_{ds}$ vs $V_{ds}$) of the device at varying gate voltages from −2 to 10 V (Figure 2c) exhibit good FET characteristics including the linear regime, cut-off regime, and saturation regime. Also, the linear $I_{ds}$-$V_{ds}$ relationship at $V_{ds}$ < 0.5 V reflects the ohmic nature of the device contacts.

In Figure 4b, the device exhibits significant clockwise gate hysteresis, resulting in distinct channel conductance states and a memory window of 3.4 V. To ensure clarity, we define the device state at zero gate voltage in the forward and backward gate transfer characteristics as LRS and HRS, respectively. The conductance ratio between these two states is 3000, and it can

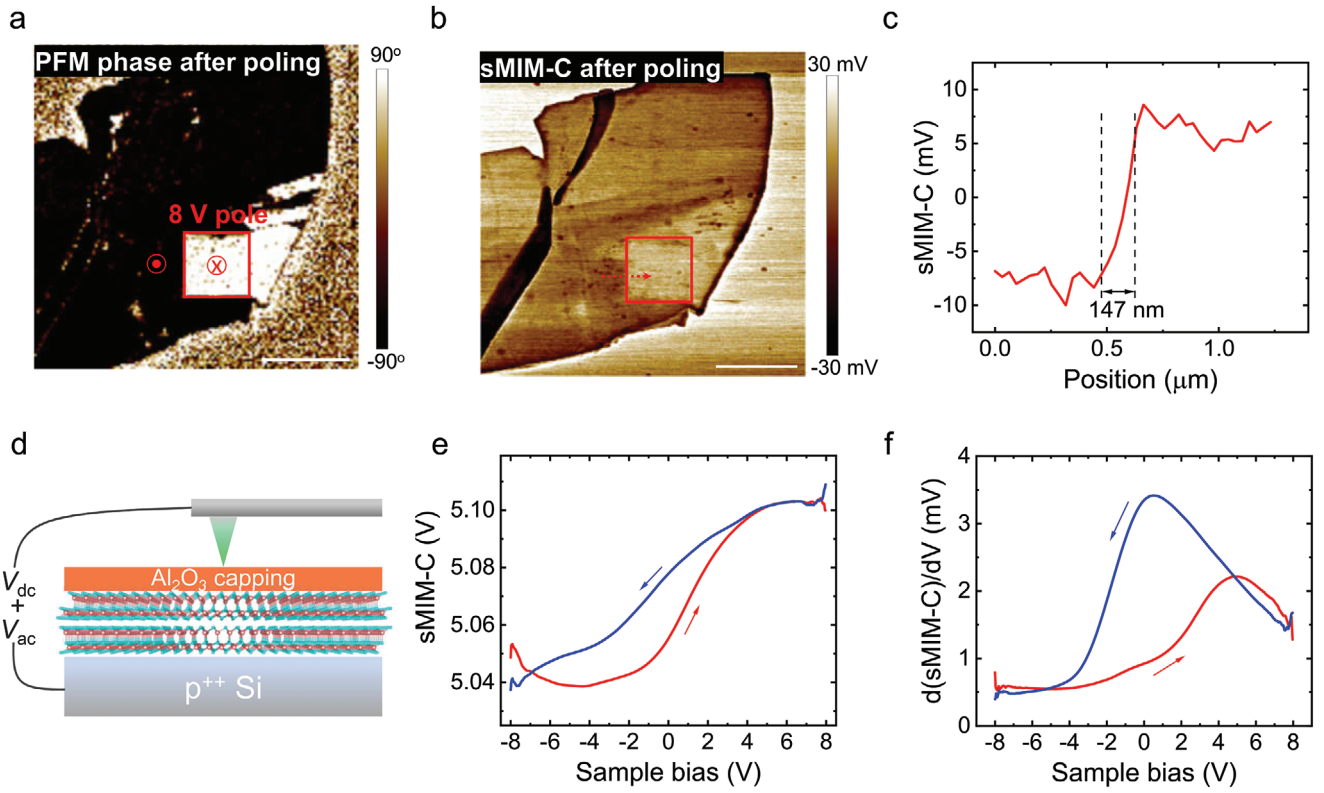


**Figure 3.** sMIM imaging of opposite $\alpha$-$In_2Se_3$ domains and sMIM-C spectroscopy of $\alpha$-$In_2Se_3$ based MOS structure. a) PFM phase image of an $\alpha$-$In_2Se_3$ flake on Si/$Al_2O_3$ substrate after poling the area indicated by the red rectangle with a tip bias of 8 V. The PFM result prior to poling process is provided in Figure S8 (Supporting Information). b) sMIM-C image of the same area in (a) reveals a contrast between domains of opposite polarization direction, indicating polarization-modulated flake conductivity. c) sMIM-C profile along the red dashed line in (b). Scale bars in (a) and (b) are 2 μm. d) The schematic experimental structure for sMIM spectroscopy. e) sMIM-C response as a function of sample bias exhibiting n-type MOS-like characteristics with additional hysteresis. f) d(sMIM-C)/dV signal in dependence of sample bias acquired with a 2000 mV AC voltage at 90 kHz applied for capacitance modulation.

even exceed $10^5$ (Figure S14, Supporting Information), indicating that $\alpha$-$In_2Se_3$ FeSFETs possess a large dynamic range and are well-suited for applications such as memories or artificial synapses.[17,18] The observed large clockwise hysteresis agrees well with the *C-V* characteristics of MOS structure in Figure 3, which is readily attributed to the gate-modulated ferroelectric polarization switching of the $\alpha$-$In_2Se_3$ channel, as illustrated in the insets of Figure 4b.

Under high negative gate voltage, the ferroelectric polarization direction (from negative bond charge to positive bond charge) points from $\alpha$-$In_2Se_3$ toward the back-gate $Al_2O_3$ dielectric. This induces positive charges at the bottom surface of $In_2Se_3$, causing the energy band to bend downward. Consequently, this results in a higher carrier density and the LRS device state after the removal of the gate bias. On the other hand, a high positive gate voltage reverses the polarization, leading to a lower charge carrier concentration and the HRS device state upon withdrawal of the gate voltage.

The hysteresis and tunable resistance states empower $\alpha$-$In_2Se_3$ FeSFETs to operate as artificial synapses.[17,18] To test this application, the gate electrode is used as the synaptic input terminal and the source current serves as the post-synaptic current. Figure 4d–f shows the ability of the device to emulate essential synaptic behaviors including excitatory post-synaptic current (EPSC), inhibitory post-synaptic current (IPSC), long-term potentiation (LTP), and long-term depression (LTD). Particularly, the EPSC and IPSC maintain their signal strength beyond 6000 s, which is indicative of the excellent non-volatility of the synapse state. In the following, we will be focused on the in situ characterization of $\alpha$-$In_2Se_3$ FeSFET by sMIM.

The AFM image of a representative device for sMIM characterization made from a 34.2-nm $\alpha$-$In_2Se_3$ nanosheet is shown in **Figure 5a** (see Figure S15, Supporting Information for a full AFM image of the device). The channel length and width are 4.2 and 4 μm, respectively. The electrical characteristics of the device are provided in Figure S14c (Supporting Information). It is worth pointing out that the presence of a capping dielectric layer will prevent access by SPM techniques such as SSRM and conductive AFM to locally characterize the device, both of which require current flowing. Figure 5b reports the sMIM-C images of the device under different gate modulation voltage of −8, 0, and 8 V. The channel at 8 V $V_{gs}$ gives rise to the highest sMIM-C signal, whereas the sMIM-C image of the channel is darkest for $V_{gs}$ = −8 V, indicating conductive and insulating limits of the channel as a result of electrostatic modulation. The differences in sMIM-C response at different gate potentials are clearly noticed from the line profiles in Figure 5c. While the sMIM signal remains unchanged for $Al_2O_3$ dielectric due to its insulating property and

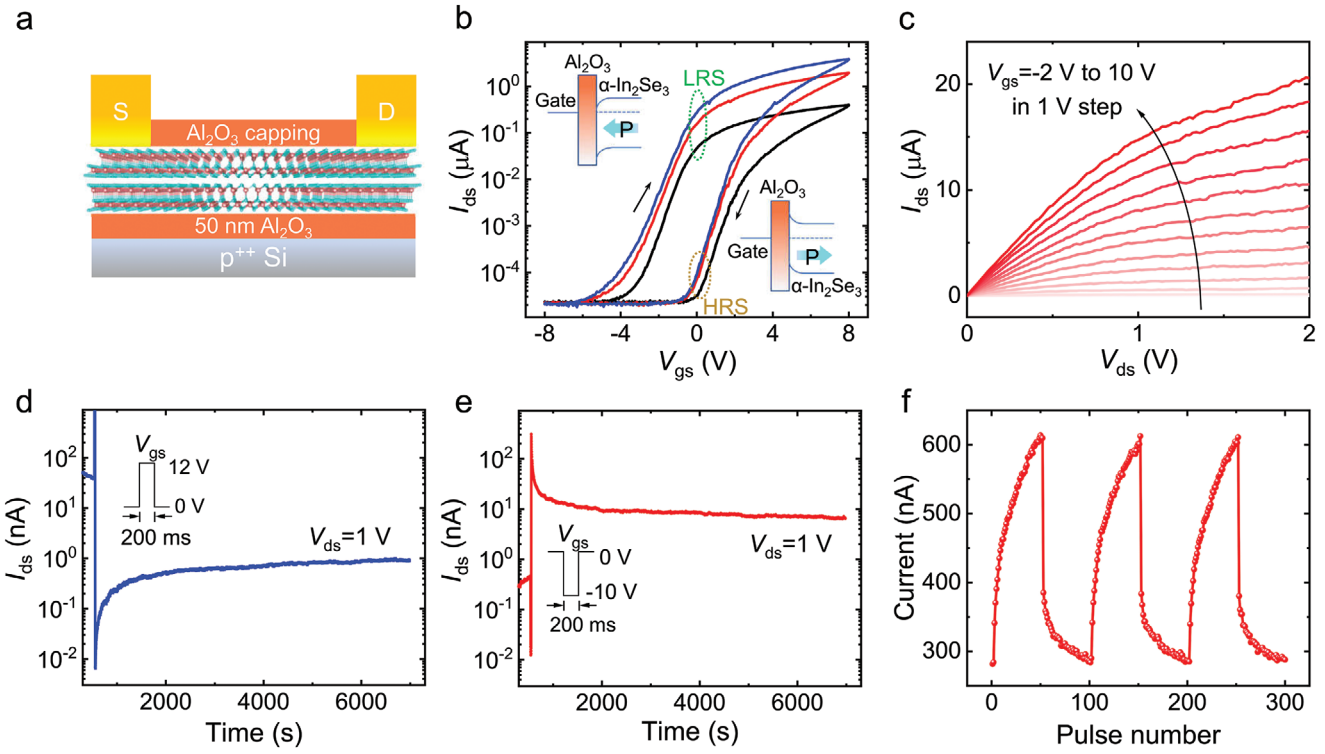


**Figure 4.** $\alpha$-$In_2Se_3$ synaptic FeSFETs. a) Schematic structure of the $\alpha$-$In_2Se_3$ FeSFETs. b) Transfer characteristics of a representative device ($L_{ch}$ = 1 μm, $W_{ch}$ = 3 μm, channel thickness = 47.2 nm) at $V_{ds}$ of 0.01, 0.05, and 0.1 V, exhibiting large clockwise gate hysteresis. Insets show energy band diagrams to illustrate the mechanism of the device HRS and LRS corresponding to different ferroelectric polarization states modulated by $V_{gs}$. c) Output characteristics of the device for $V_{gs}$ from −2 to 8 V with 1 V step. d–f) Operation of $\alpha$-$In_2Se_3$ FeSFET to emulate typical synaptic behaviors of IPSC d), EPSC (e), and LTP/LTD f). For LTP/LTD emulation, pulse trains of −5 and 3 V amplitude and 100 μs width were used. $V_{ds}$ of 0.5 V were used for monitoring channel current.

absence of gating effect, it increases with gate voltage for the $\alpha$-$In_2Se_3$ channel. Specifically, when $V_{gs}$ = −8 V, the sMIM-C for $Al_2O_3$ dielectric is larger than $\alpha$-$In_2Se_3$. This can be attributed to carrier depletion in $\alpha$-$In_2Se_3$, resulting in a decreased capacitance sensed by the probe due to the insertion of $\alpha$-$In_2Se_3$ between the tip and back-gate $Al_2O_3$. For $V_{gs}$ = 8 V, the $\alpha$-$In_2Se_3$ is switched to the accumulation regime with increased carrier density, thus giving rise to an increased sMIM-C signal. These results correspond well to the off-state regime, subthreshold regime, and on-state regime of the device, respectively, thus demonstrating the ability of sMIM for in situ monitoring of the resistance states in $\alpha$-$In_2Se_3$ FeSFET. The sMIM-C signal is uniform across the entire channel of the exfoliated monocrystalline $\alpha$-$In_2Se_3$ flake, indicating a negligible effect of coupling to nearby metals.

To monitor the evolution of the conductance state at a specific location, the sMIM-C image is collected by scanning the sample along a fixed line at various gate voltages, as shown in Figure 5d. It can be noticed that besides the contrast of sMIM-C responses at different gate voltages (see the line profiles in Figure S16, Supporting Information), the sMIM-C signal exhibits apparent variation at $V_{gs}$ = 0 V following 10 and −10 V $V_{gs}$ scans, indicating the device channel enters different states after being subjected to stimulation by different gate voltages. This is better illustrated by the two averaged line profiles in Figure 5e. Following the application of −10 V (10 V) $V_{gs}$, an increased (decreased) sMIM-C response is recorded at 0 V $V_{gs}$ for the device channel. This is in excellent agreement with our device tests, where the application of 10 and −10 V $V_{gs}$ switches the polarization of $\alpha$-$In_2Se_3$, and drives the device to its HRS and LRS, respectively. Thus, the sMIM response provides a quantitative measure of the synaptic state of synaptic $\alpha$-$In_2Se_3$ FeSFET. Furthermore, since sMIM probes the local electrical properties of the sample, it averts the impact of contact resistance toward understanding device properties, which is frequently encountered in device data analysis.[36]

In order to evaluate the conductivity modulation of the $\alpha$-$In_2Se_3$ channel from the sMIM-C results, we carried out finite element modeling of the tip-sample interaction. The conductivity-dependent microwave admittance is simulated and demodulated, as shown in Figure 5f (see Experimental section for details). It is noted that the distinct sMIM-C signal difference of ~30 mV between ±10 V gating voltage for the channel approaches the simulated sMIM-C signal range, indicating a strong modulation of the channel conductivity by the two gate potentials, which is in good agreement with the > $10^6$ current on/off ratio from device transport measurement. In addition, by comparing the measured sMIM signal with the simulated sMIM curve, the $\alpha$-$In_2Se_3$ channel conductivity at HRS and LRS (at 0 V $V_{gs}$) are derived to be $10^{-2}$ and 10 S $m^{-1}$ (red and blue bars in Figure 5f), respectively, which match well with the calculated values from FET device analysis (Table S2, Supporting Information), thus validating the capability of sMIM to monitor the local conductance evolution of $\alpha$-$In_2Se_3$ channel.

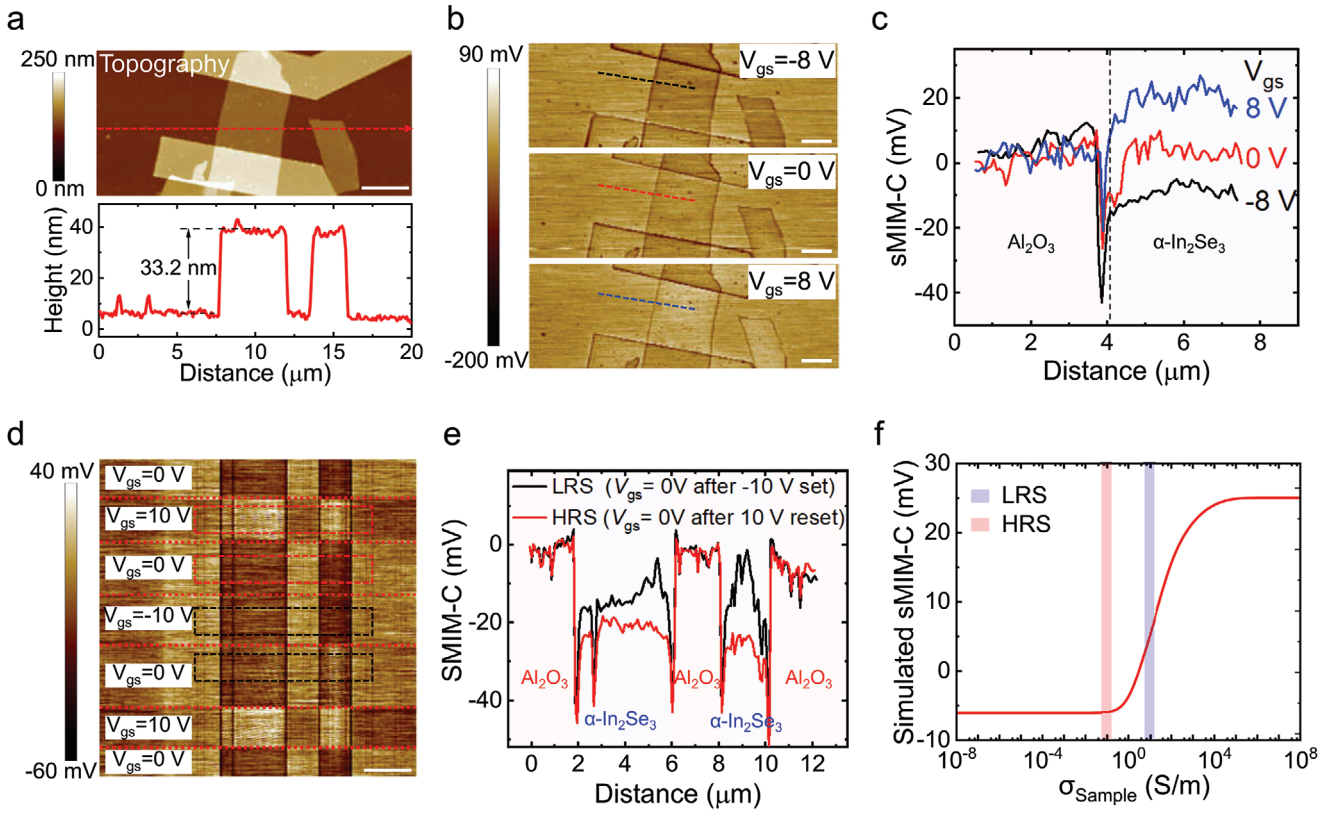


**Figure 5.** In situ sMIM characterization of $\alpha$-$In_2Se_3$ synaptic FeSFET. a) AFM topography image of the tested device and height profile of the $\alpha$-$In_2Se_3$ flakes. The scale bar is 3 μm. b) Contrasted sMIM-C images recorded at three different gate voltages of −8, 0, and 8 V, showing increased sMIM-C signal for the channel with increased $V_{gs}$. The scale bar is 2 μm. c) sMIM-C profiles along the three indicated lines in b. d) A sMIM-C image acquired by fixing the tip scan along the red arrowed line in a and varying the gate voltage at different image zones as indicated. Scale bar is 3 μm. e) Averaged sMIM-C profiles at 0 V $V_{gs}$ of the indicated areas in d, evidencing distinct sMIM responses after the device is gated by −10 and 10 V $V_{gs}$. f) FEA simulations of the tip-sample interaction with the two HRS and LRS states indicated by red and blue bars.

## 3. Conclusion

In summary, we have employed sMIM to investigate the electrical properties of the ferroelectric semiconductor $\alpha$-$In_2Se_3$ and its synaptic FeSFETs. In the absence of gate modulation, the sMIM capacitive response of $\alpha$-$In_2Se_3$ exhibits an inverse correlation with the flake thickness. Through sMIM spectroscopy, we have characterized the local *C-V* characteristics of a FET with $\alpha$-$In_2Se_3$ as the ferroelectric semiconductor chand showed that the current-voltage behavior is a consequence of its combined semiconductor and ferroelectric behavior. At the device level, sMIM enables quantitative visualization of the channel conductance state in the synaptic $\alpha$-$In_2Se_3$ FeSFETs in a non-perturbative manner. The ability of sMIM to offer in situ spatial and temporal mapping of mesoscopic electrical properties will be invaluable for understanding the dynamics of ferroic domains and enhancing the performance of ferroelectric devices.

## 4. Experimental Section

*Materials Characterization*: The Raman spectra of exfoliated $\alpha$-$In_2Se_3$ flakes were acquired using a WITec Alpha 300R Raman Spectrometer with 532 nm wavelength laser excitation and a grating of 1800 lines $mm^{-1}$. PL spectrum was collected with the flake under 633 nm laser illumination. Thicknesses of the flakes were determined by AFM scans with a Bruker Dimension Icon AFM in ScanAsyst mode or sMIM mode. PFM was carried out on $\alpha$-$In_2Se_3$ flakes exfoliated onto a Si substrate covered with e-beam deposited Au film with an excitation AC voltage of 1000 mV amplitude near the contact resonance frequency of 280 kHz. The butterfly PFM hysteresis curve and the poled AFM image were collected using an Asylum Research MFP-3D AFM system and a Bruker Dimension Icon AFM, respectively. Probes with a Pt/Ir coating layer and a spring constant of 3 N $m^{-1}$ were used for PFM.

*Device Fabrication*: $\alpha$-$In_2Se_3$ flakes were mechanically exfoliated from a bulk single crystal onto degenerate p-doped Si substrates covered with 50 nm thick ALD-grown $Al_2O_3$ for back-gated device fabrication. Electrode pattern was defined by electron beam lithography using a poly(methyl methacrylate) (PMMA) photoresist and 15 nm/65 nm Ti/Au was deposited by e-beam evaporation followed by a standard lift-off process in acetone. A 15 nm $Al_2O_3$ capping layer was synthesized on the devices for improved stability. All the $Al_2O_3$ layers were grown in a Savannah ALD system at 150 °C by using trimethylaluminum (TMA) (each pulse of 15 ms) and water (each pulse of 15 ms) as precursors.

*Electrical Characterization*: The electrical characterization of the devices was performed on a Lake Shore model CPX cryogenic probe station connected to a Keithley 4200SCS semiconductor parameter analyzer with the devices in vacuum ($< 3 \times 10^{-4}$ Torr).

*sMIM Characterization*: The sMIM experiments were carried out on a Bruker Dimension Icon AFM platform equipped with sMIM module from PrimeNano Inc. The probes for sMIM with electrically shielded cantilevers

are commercially available (sMIM-300 from PrimeNano Inc.). Peakforce tapping sMIM was used for sMIM measurements. The two output channels of sMIM correspond to the real and imaginary parts of the local sample admittance. Prior to experiments on $\alpha$-$In_2Se_3$ flakes and devices, the sMIM module is calibrated on a standard sample covered with $SiO_2$ and Al dots (with ≈4 nm native oxide). By tuning the phase shifter in front of the I-Q (in-phase and quadrature) mixer, the sMIM channels with and without contrast between $SiO_2$ and Al dots are adjusted to be sMIM-C (capacitive or imaginary parts of the local sample admittance) and sMIM-R (lossy or real parts of the local sample admittance) signal, respectively. For in situ sMIM measurements, the bias voltages applied to the drain and gate electrodes are separately supplied by a Keithley 2400 SMU, with the source electrode being grounded. FEA simulations are conducted using the commercial software COMSOL 4.4. Details of the FEA are provided in Supporting Information. The conversion between demodulated tip-sample admittance and the sMIM-C output is based on a calibration procedure similar to the work in Ref.[28,36]

*Statistical Analysis*: The sMIM-C response of $\alpha$-$In_2Se_3$ flakes with different thicknesses were obtained from 8 regions on a sample. The number of samples for sMIM-C spectroscopy and d(sMIM-C)/dV amplitude response test was 4 in Figure 3 and Figure S9 (Supporting Information). 6 FeSFETs were tested and the results were shown in Figure 4 and Figure S14 (Supporting Information).

## Supporting Information

Supporting Information is available from the Wiley Online Library or from the author.

## Acknowledgements

L.W. and H.C. contributed equally to this work. L.W. acknowledges the support from the National Natural Science Foundation of China (Grant No. 52302187). K.P.L. acknowledges support from the Hong Kong Jockey Club Global STEM professorship project BDA6 and project P0043063. L.W. thanks Prof. Lai Keji at the University of Texas at Austin for valuable discussion on the work.

## Conflict of Interest

The authors declare no conflict of interest.

## Data Availability Statement

The data that support the findings of this study are available from the corresponding author upon reasonable request.

## Keywords

ferroelectric semiconductor, finite element analysis, neuromorphic device, scanning microwave impedance microscopy, $\alpha$-$In_2Se_3$

Received: December 25, 2023
Revised: February 26, 2024
Published online: March 13, 2024

[1] S. Li, F. Wang, Y. Wang, J. Yang, X. Wang, X. Zhan, J. He, Z. Wang, *Adv. Mater.* **2023**, *35*, 2301472.
[2] F. Xue, J.-H. He, X. Zhang, *Appl. Phys. Rev.* **2021**, *8*, 021316.
[3] D. W. Zhang, P. Schoenherr, P. Sharma, J. Seidel, *Nat. Rev. Mater.* **2023**, *8*, 25.
[4] Z. Guan, H. Hu, X. Shen, P. Xiang, N. Zhong, J. Chu, C. Duan, *Adv. Electron. Mater.* **2019**, *6*, 1900818.
[5] M. Wu, *ACS Nano* **2021**, *15*, 9229.
[6] C. Wang, L. You, D. Cobden, J. Wang, *Nat. Mater.* **2023**, *22*, 542.
[7] C. Cui, F. Xue, W.-J. Hu, L.-J. Li, *npj 2D Mater. Appl.* **2018**, *2*, 18.
[8] W. Han, X. Zheng, K. Yang, C. S. Tsang, F. Zheng, L. W. Wong, K. H. Lai, T. Yang, Q. Wei, M. Li, W. F. Io, F. Guo, Y. Cai, N. Wang, J. Hao, S. P. Lau, C. S. Lee, T. H. Ly, M. Yang, J. Zhao, *Nat. Nanotechnol.* **2023**, *18*, 55.
[9] W. Ding, J. Zhu, Z. Wang, Y. Gao, D. Xiao, Y. Gu, Z. Zhang, W. Zhu, *Nat. Commun.* **2017**, *8*, 14956.
[10] F. Xue, W. Hu, K. C. Lee, L. S. Lu, J. Zhang, H. L. Tang, A. Han, W. T. Hsu, S. Tu, W. H. Chang, C. H. Lien, J. H. He, Z. Zhang, L. J. Li, X. Zhang, *Adv. Funct. Mater.* **2018**, *28*, 1803738.
[11] F. Liu, L. You, K. L. Seyler, X. Li, P. Yu, J. Lin, X. Wang, J. Zhou, H. Wang, H. He, S. T. Pantelides, W. Zhou, P. Sharma, X. Xu, P. M. Ajayan, J. Wang, Z. Liu, *Nat. Commun.* **2016**, *7*, 12357.
[12] Z. Chen, W. Fu, L. Wang, W. Yu, H. Li, C. K. Y. Tan, I. Abdelwahab, Y. Shao, C. Su, M. Sun, B. Huang, K. P. Loh, *Adv. Sci.* **2021**, *8*, e2100713.
[13] M. Si, A. K. Saha, S. Gao, G. Qiu, J. Qin, Y. Duan, J. Jian, C. Niu, H. Wang, W. Wu, S. K. Gupta, P. D. Ye, *Nat. Electron.* **2019**, *2*, 580.
[14] M. Si, Z. Zhang, S. C. Chang, N. Haratipour, D. Zheng, J. Li, U. E. Avci, P. D. Ye, *ACS Nano* **2021**, *15*, 5689.
[15] Y. Zhang, L. Wang, H. Chen, T. Ma, X. Lu, K. P. Loh, *Adv. Electron. Mater.* **2021**, *7*, 2100609.
[16] K. Liu, T. Zhang, B. Dang, L. Bao, L. Xu, C. Cheng, Z. Yang, R. Huang, Y. Yang, *Nat. Electron.* **2022**, *5*, 761.
[17] S. Wang, L. Liu, L. Gan, H. Chen, X. Hou, Y. Ding, S. Ma, D. W. Zhang, P. Zhou, *Nat. Commun.* **2021**, *12*, 53.
[18] L. Wang, X. Wang, Y. Zhang, R. Li, T. Ma, K. Leng, Z. Chen, I. Abdelwahab, K. P. Loh, *Adv. Funct. Mater.* **2020**, *30*, 2004609.
[19] R. Quhe, Z. Di, J. Zhang, Y. Sun, L. Zhang, Y. Guo, S. Wang, P. Zhou, *Nat. Nanotechnol.* **2023**, *19*, 173.
[20] S. Berweger, J. C. Weber, J. John, J. M. Velazquez, A. Pieterick, N. A. Sanford, A. V. Davydov, B. Brunschwig, N. S. Lewis, T. M. Wallis, P. Kabos, *Nano Lett.* **2015**, *15*, 1122.
[21] S. Berweger, G. Qiu, Y. Wang, B. Pollard, K. L. Genter, R. Tyrrell-Ead, T. M. Wallis, W. Wu, P. D. Ye, P. Kabos, *Nano Lett.* **2019**, *19*, 1289.
[22] Y. Liu, R. Ghosh, D. Wu, A. Ismach, R. Ruoff, K. Lai, *Nano Lett.* **2014**, *14*, 4682.
[23] K. Lai, W. Kundhikanjana, M. Kelly, Z. X. Shen, *Rev. Sci. Instrum.* **2008**, *79*, 063703.
[24] O. Amster, F. Stanke, S. Friedman, Y. Yang, S. J. Dixon-Warren, B. Drevniok, *Microelectron. Reliab.* **2017**, *76–77*, 214.
[25] X. Sun, Y. Chen, Z. Li, Y. Han, Q. Zhou, B. Wang, T. Taniguchi, K. Watanabe, A. Zhao, J. Wang, Y. Liu, J. Xue, *ACS Nano* **2021**, *15*, 16314.
[26] Y. L. Huang, L. Zheng, P. Chen, X. Cheng, S. L. Hsu, T. Yang, X. Wu, L. Ponet, R. Ramesh, L. Q. Chen, S. Artyukhin, Y. H. Chu, K. Lai, *Adv. Mater.* **2020**, *32*, 1905132.
[27] X. Huang, L. Chen, S. Tang, C. Jiang, C. Chen, H. Wang, Z. X. Shen, H. Wang, Y. T. Cui, *Nano Lett.* **2021**, *21*, 4292.
[28] D. Wu, W. Li, A. Rai, X. Wu, H. C. P. Movva, M. N. Yogeesh, Z. Chu, S. K. Banerjee, D. Akinwande, K. Lai, *Nano Lett.* **2019**, *19*, 1976.
[29] D. Wu, A. J. Pak, Y. Liu, Y. Zhou, X. Wu, Y. Zhu, M. Lin, Y. Han, Y. Ren, H. Peng, Y. H. Tsai, G. S. Hwang, K. Lai, *Nano Lett.* **2015**, *15*, 8136.
[30] D. Wu, X. Li, L. Luan, X. Wu, W. Li, M. N. Yogeesh, R. Ghosh, Z. Chu, D. Akinwande, Q. Niu, K. Lai, *Proc. Natl. Acad. Sci. U S A* **2016**, *113*, 8583.
[31] K. Lee, M. I. B. Utama, S. Kahn, A. Samudrala, N. Leconte, B. Yang, S. Wang, K. Watanabe, T. Taniguchi, M. V. P. Altoe, G. Zhang, A. Weber-

Bargioni, M. Crommie, P. D. Ashby, J. Jung, F. Wang, A. Zettl, *Sci. Adv.* **2020**, *6*, eabd1919.
[32] G. Anderson, *Microsc. Today* **2013**, *21*, 32.
[33] K. Lai, H. Peng, W. Kundhikanjana, D. T. Schoen, C. Xie, S. Meister, Y. Cui, M. A. Kelly, Z.-X. Shen, *Nano Lett.* **2009**, *9*, 1265.
[34] J. Yu, Y. Zhou, X. Wang, A. Dodabalapur, K. Lai, *Nano Lett.* **2023**, *23*, 11749.
[35] X. Wu, Z. Hao, D. Wu, L. Zheng, Z. Jiang, V. Ganesan, Y. Wang, K. Lai, *Rev. Sci. Instrum.* **2018**, *89*, 043704.
[36] Y. Zhao, K. Xu, F. Pan, C. Zhou, F. Zhou, Y. Chai, *Adv. Funct. Mater.* **2017**, *27*, 1603484.